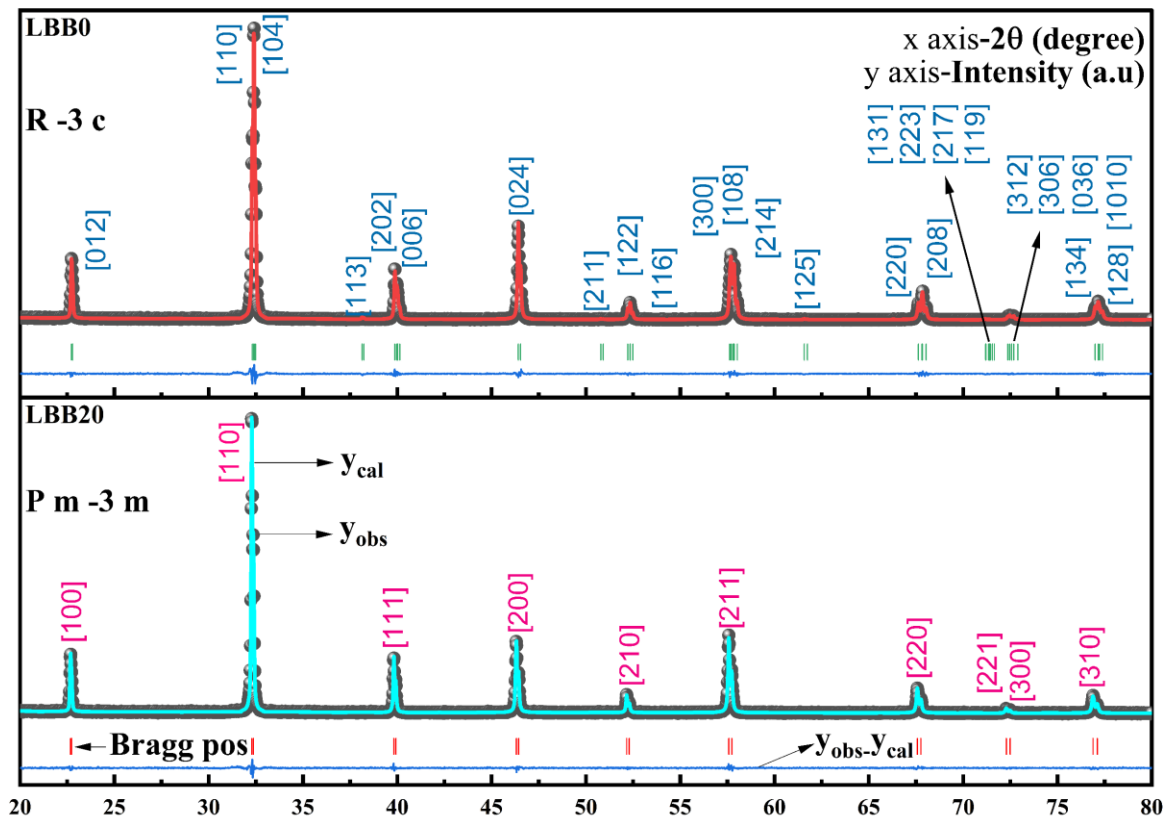


These days any diffraction data can be handled using whole powder pattern fitting which includes whole powder pattern decomposition (WPPD, also called as profile matching) and Reitveld analysis (also called as structure matching)<sup>1</sup>. The latter uses Wyckoff position of the atoms, their isotropic Debye-Waller factors, and the occupancies to calculate the intensities and to generate the powder pattern to compare with the obtained one. In contrast WPPD doesn't require any prior knowledge of atomic attributes. The WPPD includes two methods viz. The Pawley method and the Le Bail method (LB). The Le Bail method is most often used WPPD method which begins with arbitrary values of intensities which evolve iteratively upon assigning to estimates of divided data amongst the contributing reflections. In this method, estimates to cell parameters, peak profile parameters, zero shift of the sample and background function can also be obtained along with the with the Le Bail intensity extraction. The advantage of LB is that it is the only way to intensity extraction when structure is unknown or vague. Also, LB is preferential over Rietveld method when experimental artefacts are difficult to model, as may be the case in situ diffraction. The WPPD is becoming increasing popular as its can be a precursor for structure matching. Say when the structural model is very crude, it is advisable to analyse the pattern first with the LB to obtain the cell parameters, profile shape function and, background before running the Rietveld refinement. However, as the constraint used in WPPD are few and simpler compared to Rietveld method, it more prone to give ambiguous results if profile shape parameters or microstructural parameters are refined<sup>2</sup>.

The WPPD using LB is performed using EDPCR utility of fullprof software. The input files such as the crystallography information file (.cif file), datafile (.dat file), and background file (bgr.file) are supplied to input control file (.pcr file) which manipulates various command supplied by the user within the framework of the fullprof program. Initially a cif file is supplied to the EDPCR to convert it into a pcr file. The file contains the approximate information such as lattice parameters, space group etc. of a hypothesized structure based on the pre-refinement

assessment of the diffraction pattern. Pcr demands several inputs like the dat file which can be in free format or X, Y, SIGMA format. The wavelengths of the x-ray ( $\lambda_1=1.540560\text{\AA}$ ,  $\lambda_2=1.544390\text{\AA}$ , and  $I_1/I_2 = 0.5$ ), peak shape function (Thompson-Cox-Hastings pseudo-Voigt \* Axial divergence asymmetry) and background type (linear interpolation between a set of background points with refinable heights). User must invoke profile matching with constant scale factor for calculation over EDPCR platform or job=2 over winplotr platform. The program extracts intensities upon iteration (not exceeding 10) and will be available in output file (.hkl file). If the supplied model is exact model, all the peaks will be accounted upon decomposition in the whole pattern otherwise a missing bragg position will be seen upon plotting the .PRF file. Thus, a confirmation on crystal structure without a prior knowledge of atomic attributes and precursor for Rietveld analysis can be obtained from the Le Bail fitting.



**Figure s1. The Le bail fitted XRD patterns of LBB0 and LBB20 as a sample for each space group. The graph contains observed data, calculate data, difference curve and Bragg reflections. The (hkl) values corresponding to each Bragg position are shown above the respective peak.**

**Table s1: The space group used for profile matching, the lattice parameters obtained and reliability factors of Le Bail fitting.**

Sample code P.Q	LBB0	LBB5	LBB10	LBB20	LBB30	LBB40
Space group	R -3 c	R -3 c	R -3 c	P m -3 m	P m -3 m	P m -3 m
$a=b$ in Å	5.537	5.538	5.541	3.918	3.922	3.926
$c$ in Å	13.504	13.513	13.527			
$V$ in Å <sup>3</sup>	358.516	358.931	359.649	60.141	60.316	60.518
$R_{wp}$	13.1	12.2	12.2	10.4	10.8	9.25
$R_{exp}$	10.72	10.12	9.83	9.63	8.62	8.01
$\chi^2$	1.48	1.46	1.54	1.17	1.58	1.33
$R_B$	0.583	0.741	0.692	0.457	0.621	1.25

The possible space group, lattice parameters, the reliability factors and  $\chi^2$  are tabulated in table s1. In principle the difference profile plot (difference curve) is the best way to validate the Le bail fitting and Reitveld refinement, however there can be numerical parameter which would authenticate the good fit which are called as reliability factors or agreement indices or R values.

Such R values are the weighted-profile R value ( $R_{wp}$ ), the statistically expressed R value ( $R_{exp}$ ), the Bragg-intensity R value ( $R_B$ ). As the  $R_{wp}$  is background sensitive always is preferential to have this value without the background contribution. Ideally for a best fit the  $R_{wp}$  must approach  $R_{exp}$  and the  $R_B$  must be small but positive value. The ratio of  $R_{wp}$  to  $R_{exp}$  ( $R_{wp}/R_{exp} = \chi^2$ ) should approach to unity for a best fit but this value depends on  $R_{exp}$ . Suppose the data is over collected,  $R_{exp}$  will be very small and consequently the  $\chi^2$  will quite larger than 1 and conversely for a under collected data  $R_{exp}$  will be very large and hence  $\chi^2$  will less than 1. So, it is wise to consider the R vales and their proximity to each other, then the ratio of them. Further  $R_{wp}$  obtained for a structure free fitting (Le Bail fitting) is excellent indicator of best fit and should approach the statistically expected R value. Also, the  $R_{wp}$  Reitveld refinement must agree with the  $R_{wp}$  of LB<sup>3</sup>.

The straight-line nature of the difference curve with minimal spikes at some reflections, the small difference between the  $R_{wp}$  and  $R_{exp}$ , the value of  $\chi^2$  close to unity and small values of  $R_B$  are indicators of good agreement between the experimental and calculated data governed by proposed space group. So, it is confirmed that the specimen LBB0, LBB5, LBB10 belong to rhombohedral structure and LBB20, LLB30, and LBB40 belong to cubic crystal system. The corresponding (hkl) values are tabulated in table s2 consisting of respective 2 $\theta$  values.

**Table s2: The HKL values and corresponding 2 $\theta$  value for each sample.**

(hkl)	2 $\theta$ in degree			(hkl)	2 $\theta$ in degree		
	LBB0	LBB5	LBB10		LBB20	LBB30	LBB40
0 1 2	22.727	22.718	22.702	1 0 0	22.677	22.655	22.629
1 1 0	32.311	32.302	32.287	1 1 0	32.287	32.254	32.218
1 0 4	32.406	32.389	32.36	1 1 1	39.818	39.778	39.732
1 1 3	38.131	38.117	38.092	2 0 0	46.309	46.261	46.207

2 0 2	39.868	39.856	39.834	2 1 0	52.159	52.105	52.043
0 0 6	40.027	40.001	39.956	2 1 1	57.577	57.516	57.446
0 2 4	46.415	46.396	46.363	2 2 0	67.57	67.496	67.411
2 1 1	50.787	50.773	50.747	3 0 0	72.287	72.206	72.113
1 2 2	52.217	52.2	52.172	2 2 1	72.287	72.206	72.113
1 1 6	52.345	52.318	52.271	3 1 0	76.883	76.795	76.694
3 0 0	57.623	57.607	57.578				
2 1 4	57.684	57.662	57.624				
0 1 8	57.864	57.827	57.763				
1 2 5	61.573	61.548	61.503				
2 2 0	67.627	67.606	67.571				
2 0 8	67.846	67.807	67.74				
1 3 1	71.185	71.162	71.124				
2 2 3	71.211	71.187	71.145				
2 1 7	71.345	71.31	71.248				
1 1 9	71.453	71.408	71.331				
3 1 2	72.362	72.339	72.298				
0 3 6	72.469	72.436	72.38				
3 0 6	72.469	72.436	72.38				
1 0 10	72.682	72.631	72.544				
1 3 4	77.002	76.973	76.924				
1 2 8	77.158	77.117	77.044				

ImageJ is a Java based open-source software first developed by Wayne Rasband for image processing. Presently it has large number of user defined macros and 400+ plugins

utilised in the field of material science, medical imaging and engineering. ImageJ supports a wide number of standard image file formats, including the recent implementation 48-bit color composite image support. It incorporates various useful tools including reading and writing of image files. Handling individual pixels, image regions, whole image or even volumes. It performs deconvolution, edge detections, particle analysis, histogram manipulation, Fourier transforms and standard image filtering. It can even perform mathematical operations such as multiplication and division. It does a remarkable background subtraction routine for uneven background and support various user written plugins. It supports many automated image segmentation algorithms like ostu thresholding, mixture modelling, maximum entropy, colour-based thresholding and K-means clustering<sup>4-9</sup>.

An FESEM image of concern is opened using in Image J and sharpened (processes tab) for better visualization of grains and grain boundaries. To begin with particle analysis, it is essential to convert the scale from pixel to micrometer ( $\mu\text{m}$ ) or nano meter (nm). A straight-line tool of the tool bar is chosen, and an appropriate scale is selected (shift+draw) to set the scale. For instance, a  $2\mu\text{m}$  line which is given in the image selected. The analyse tab in the main menu has set scale tool where the know distance is change to 2 and unit of length is changed to um so that the present scale will be pixel/ $\mu\text{m}$ . One can use analyse particle utility in the analyse tab of the main menu to calculate the area. Area%, standard deviation, perimeter etc after thresholding. But thresholding can some time reap ambiguous data if the selected area of the image is subjected to poor thresholding. Instead, it is better to select the individual grain or particles using freehand selection tool in the tool bar. Shortcut B+M will allow the measurement and allows the user to visualise the traced area for future references. A datasheet will be created upon measurement, which can be exported for statistical analysis (see figure s2). Followed by the particle size analysis the porosity analysis can be carried out for the same image. An unprocessed image is again chosen for analysis and same steps are

followed up to set scale. Followed is thresholding of image. The image tab of the main menu has a tool called adjust, which contains thresholding (ctrl+shift+T) utility. The default (red) mode of the lower threshold is set to zero and upper threshold is varied so that only the pores are highlighted (care must be taken not to high light the grains). After thresholding the measurement is carried out to find the area% which is indicator of porosity in each (selected) area<sup>10,11</sup>.

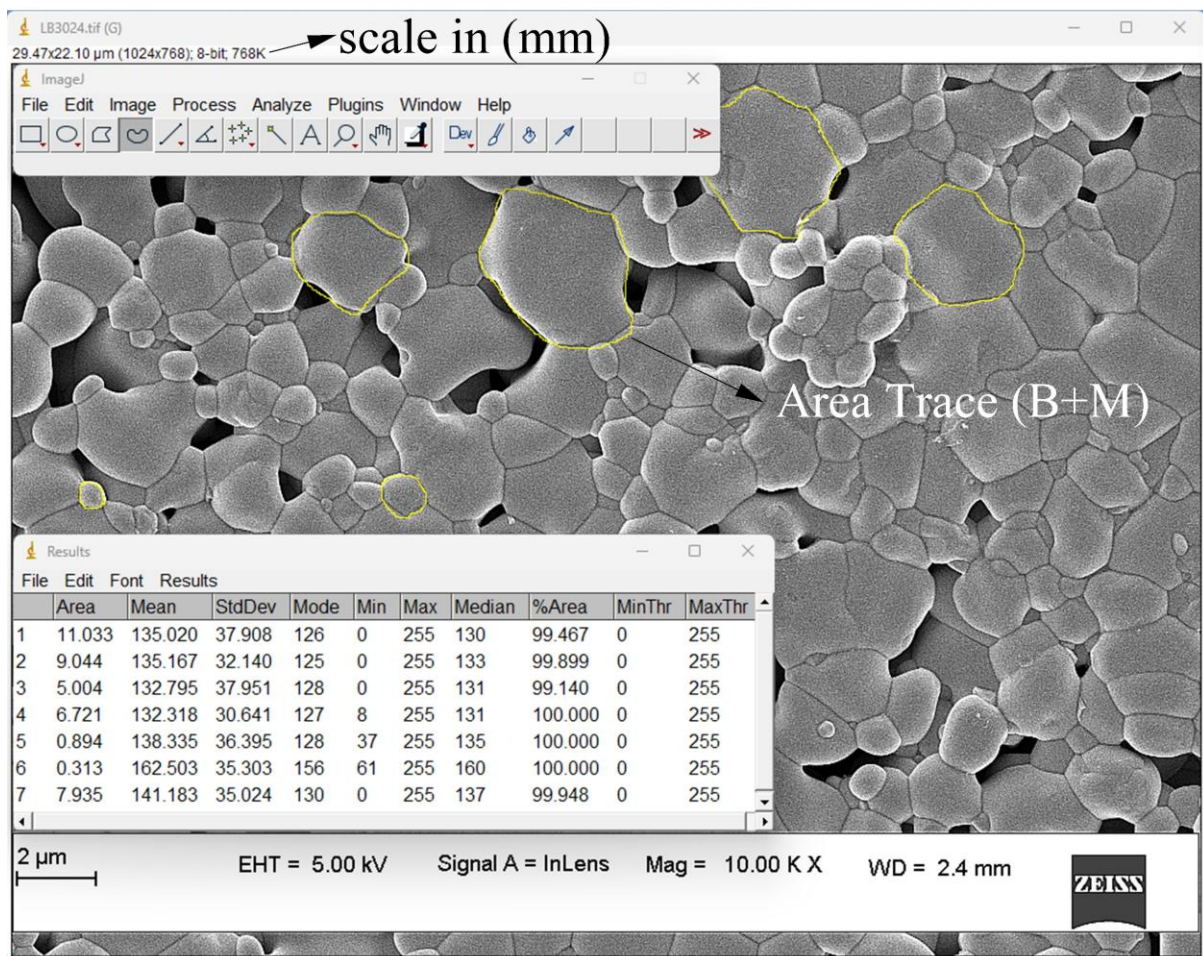


**Figure s2.** The visual picture of area trace. Tab at the left top corner is ImageJ consisting of all the tools, plugins and macros. The tab at the bottom left is the result tab containing the datasheet which can be save for further statistical analysis.

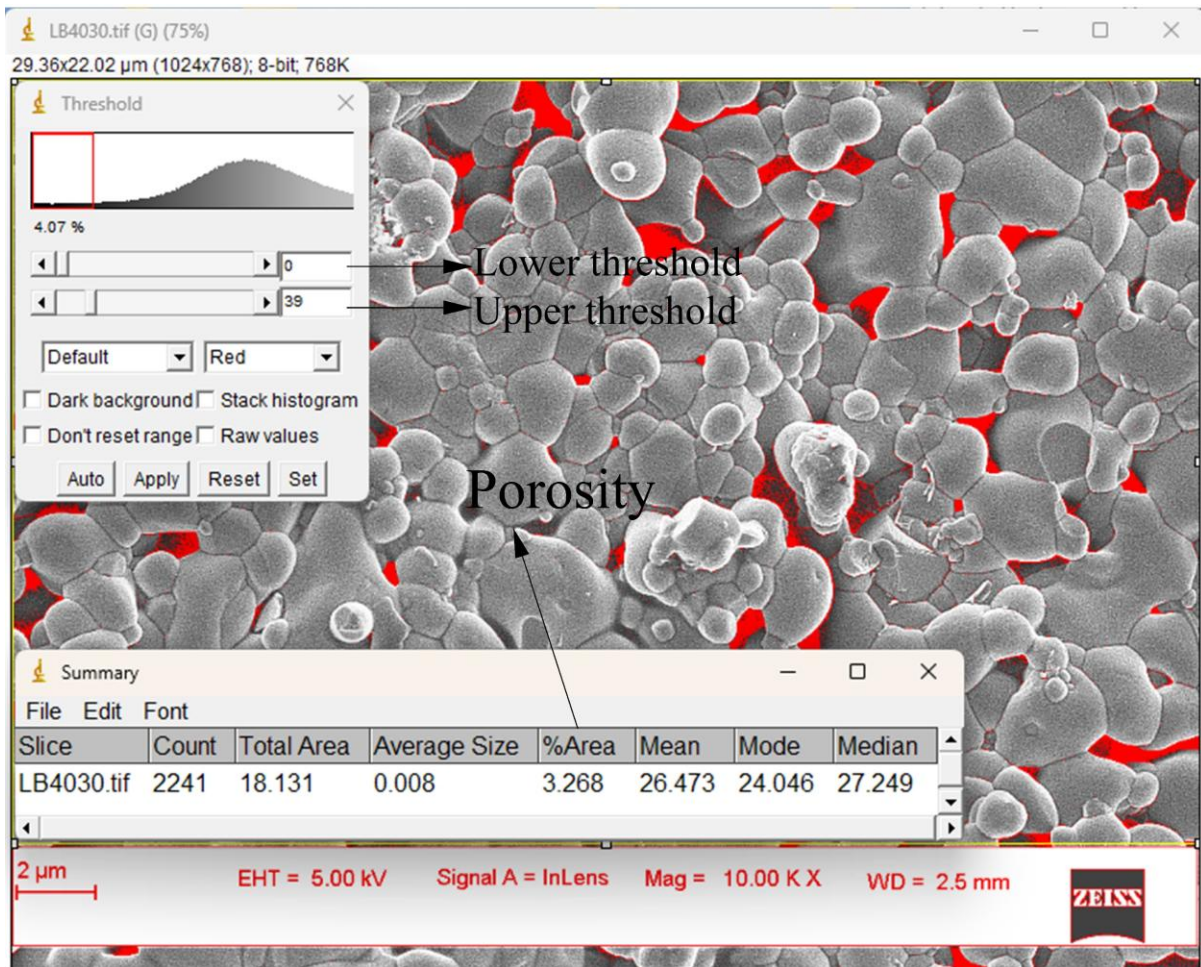


**Figure s3. The visual picture of porosity estimation. Tab at the left top corner is threshold which prompts the thresholding. The tab at the bottom left is the summary tab containing the data where area% is porosity.**

Once the data sheet on area is obtained the data was subjected to statistical analysis. A multitude of physical process such as particle size distribution, molar mass distribution, concentration of rare earths in a mineral, growth of the crystal in chemical reaction, size of ice crystals in frozen medium etc. follow lognormal distribution, or in other words, effects that are multiplicative result in lognormal distribution<sup>12</sup>. Plenty of research works consider the particle size distribution to be lognormal distribution based on model of coagulation of Smoluchowsky. This model deals with a closed system where initially large number of fine particles meet at random to coagulate<sup>13</sup>. It is an ideal treatment and doesn't map into real situations. The

coagulation model assumes the lognormality but doesn't explain its origin. However, few recent works have concluded that the origin of lognormality in particle growth distribution lies in time spent for growth. This is true in any growth process where the fundamental mechanism is diffusion and drift through a finite growth region<sup>14</sup>. Accordingly, the rate at which particle mass, and hence the particle volume  $V$  changes due to atomic absorption is proportional to the surface area. Further the particle residence time in the active zone is lognormally distributed when the particle transport occurs by means of diffusion and drift<sup>13</sup>. Sometime the description of grain size distribution using lognormal distribution lacks physical basis and researchers tend to use gamma distribution to discuss the particle size distribution. But if the distribution is narrow both the distributions secure similar results<sup>12,15</sup>. The lognormal distribution and the gamma distribution were used to describe the distribution of the grain size of in a given specimen. These two distributions are most widely used distribution for deducing particle size in polycrystalline materials<sup>16</sup>. The probability density function of a lognormal distribution is defined as  $f(x) = \frac{1}{\sqrt{2\pi}ax} \exp\left(-\frac{1}{2}\left(\frac{\ln(x)-b}{a}\right)^2\right)$  where  $x$  is data ( $0 < x < \infty$ ) whose natural logarithms are normally distributed.  $B$  is shape or mean ( $\mu$ ) of lognormal distribution and  $A^2$  ( $\sigma^2$ ) is its variance or scale. The expectation value or arithmetic mean of  $x$  is given by  $e^{b+\frac{1}{2}a^2}$ , where  $e^b$  is the geometric mean or median of the lognormal destitution (mean of corresponding normal distribution) and  $e^{a^2}$  is geometric variance. The mode of  $x$  is  $e^{b-a^2}$ , the standard deviation is  $e^{b+\frac{1}{2}a^2} \sqrt{e^{a^2} - 1}$  and variance is  $e^{2b+a^2}(e^{a^2} - 1)$ .

Similarly, the probability density function of a gamma distribution for variable  $x$  is given by  $f(x) = \frac{1}{\Gamma(k)\theta^k} x^{k-1} e^{-\frac{x}{\theta}}$ , here  $k$  designated as shape,  $\theta$  is called as scale of the gamma distribution and  $\Gamma(k)$  is gamma function. Expectation value or mean of the distribution is given by  $k\theta$ , mode is  $(k - 1)\theta$  for  $k \geq 1$  and variance is  $k\theta^2$ . Given a data, to estimate the grain size, a graphical technique called probability plots were used. In this technique, the data are plotted

against a theoretical distribution so that the points form a straight line. Deviation from this straight line indicate departures from the specified distribution. Or to be more precise the percentile of the data (area percentile) should follow the reference line and lie well within the 95% confidence band of upper and lower percentile. The shape and scale parameters of the distribution are given by the intercept and slope of the straight line. But prior to the probability plot analysis to verify underlying distribution, the natural logarithm of dataset is obtained. If the log of the random variables is normal or symmetric, the underlying distribution is lognormal distribution and if it is left skewed (depending on the shape parameter), the distribution is gamma distribution. An example probability plot for lognormal and gamma distribution and histograms of logarithm of the dataset indicating a lognormal and gamma distribution is shown in figure s4 and s5 respectively.

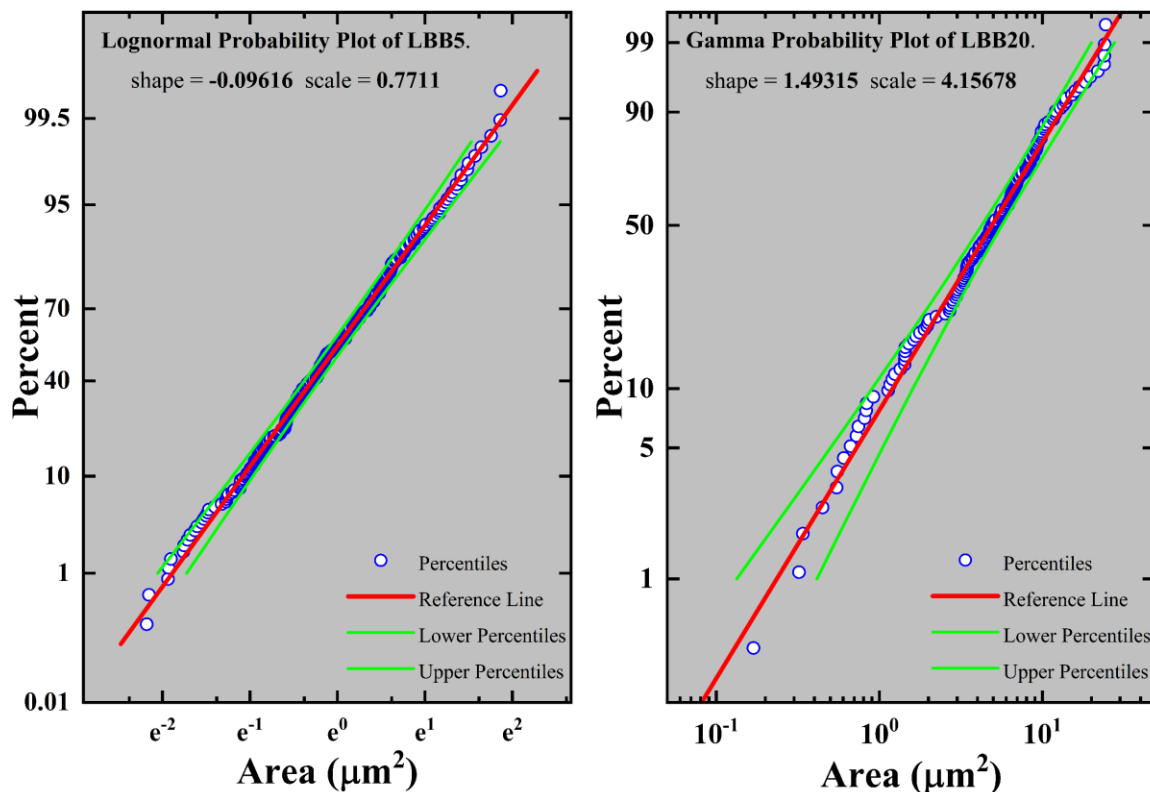


**Figure s4. The probability plots of LBB5 and LBB20 shown as a typical example of lognormal and gamma distribution.**

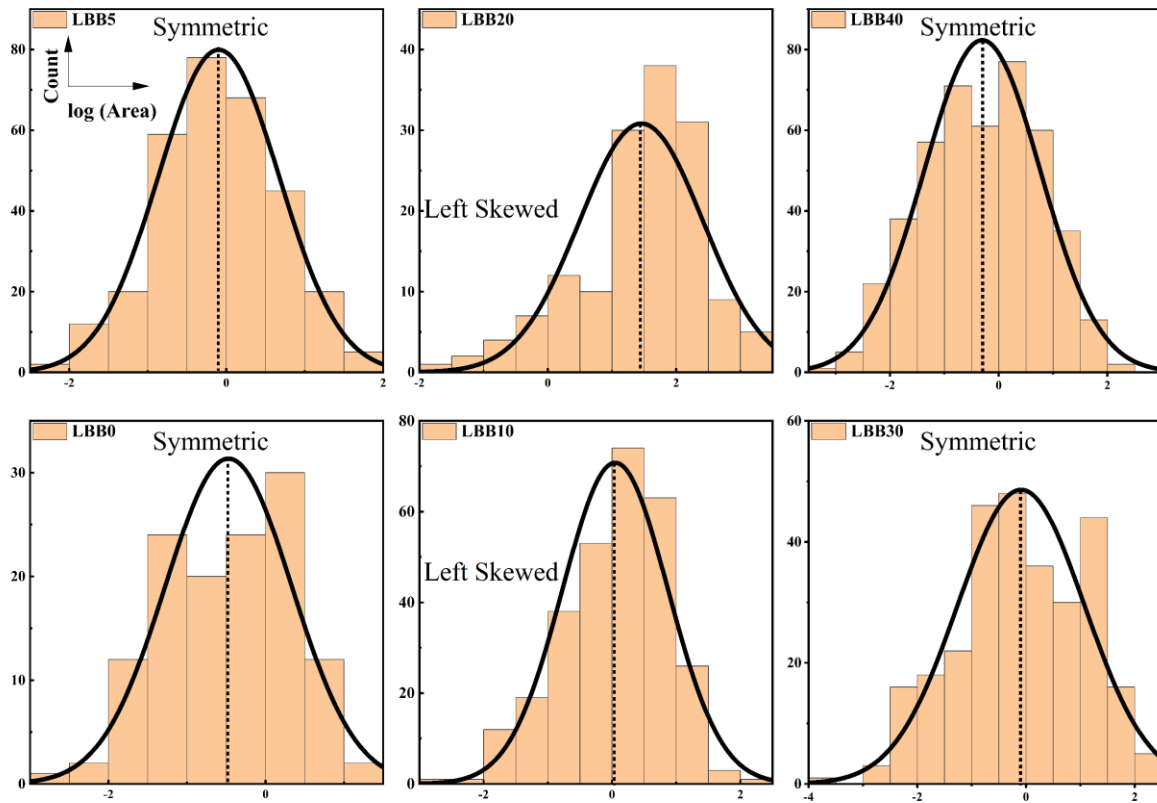


**Figure s5. The histograms and normal distribution curve of log of random variables obtained from area trace measurement. The distribution curves of logarithms of area of LBB0, LBB5, LBB30, and LBB40 are symmetric, whereas LBB10 and LBB20 are left skewed implying that the underlying distributions are lognormal and gamma respectively.**

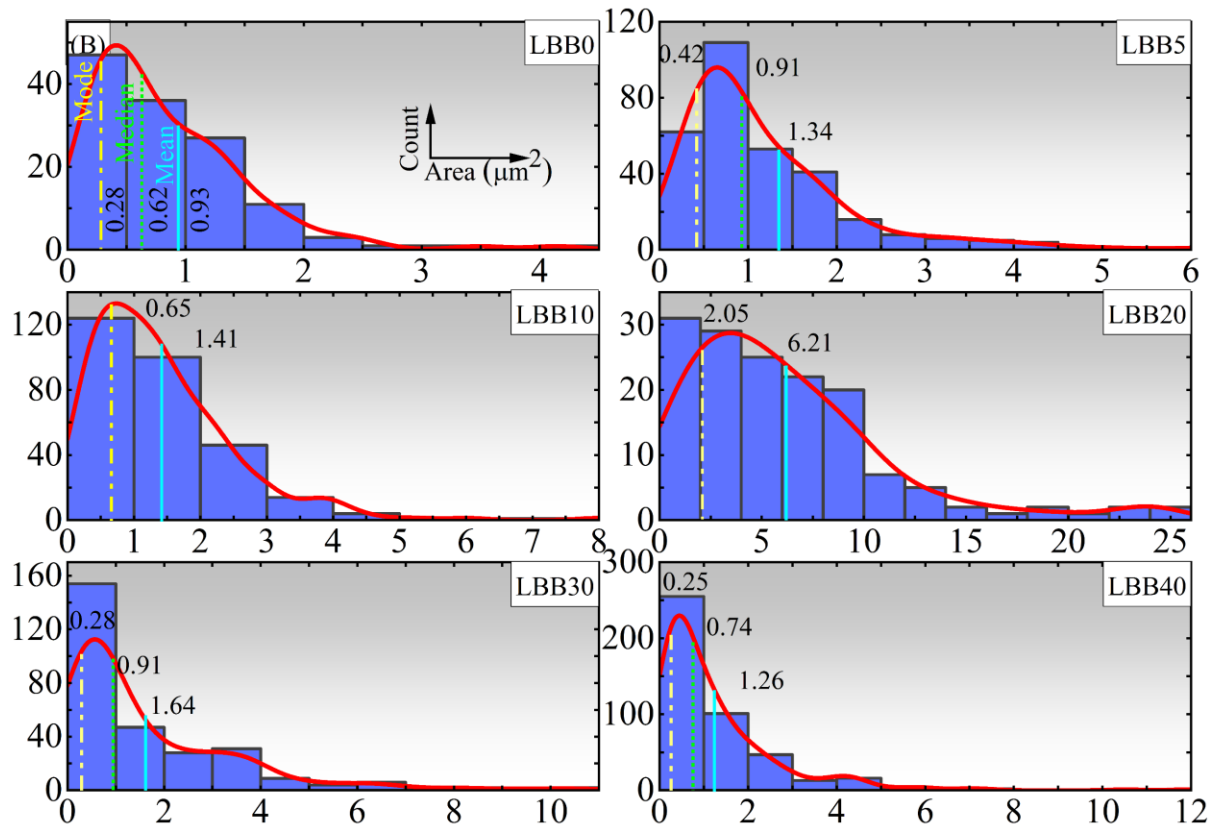


**Figure s6. Grain size distribution LBB0, LBB5, LBB30, LBB40 are in lognormal whereas LBB10, LBB20 follow gamma distribution. The columns are counts per scale; the curve is kernel smooth of respective distribution.**

**Table s3: statistical parameters of lognormal distribution**

Bi %	shape ( $\mu$ )	scale ( $\sigma^2$ )	Mean	Median	Mode	SD	Variance
0	-0.4719	0.808	0.934	0.624	0.278	1.042	1.086
5	-0.09616	0.7711	1.336	0.908	0.420	1.440	2.073
30	-0.09114	1.16965	1.638	0.913	0.283	2.442	5.961
40	-0.30482	1.0711	1.260	0.737	0.253	1.745	3.044

E(x)= Expectation value or Mean, SD= Standard Deviation

**Table s4: statistical parameters of gamma distribution**

Bi %	Shape ( $k$ )	scale ( $\theta$ )	Mean	Median	Mode	Variance	SD
10	1.857	0.758	1.407	-	0.649	1.067	1.033
20	1.493	4.157	6.207	-	2.050	25.80	5.079

E(x)= Expectation value or Mean, SD= Standard Deviation

Under normal conditions the structure of any perovskite is highly susceptible to substitution and/or vacancies (off stoichiometry at A, B and/or X site) perhaps intentional or a consequence of volatility. A substitution of ions distorts the lattice, and the lattice would undergo structural change to maintain the charge neutrality<sup>17-19</sup>. The perovskite oxides are usually processed through solid-state reaction which happens at essentially high temperatures. At these high temperatures some precursors undergo spontaneous evaporation. Bi<sub>2</sub>O<sub>3</sub> is one such compound whose melting point is relatively low compared to other precursors used in this study<sup>20,21</sup>. Even though the measures are taken by adding excess of Bi<sub>2</sub>O<sub>3</sub> during the synthesis, the limited solubility and moderately high reaction temperature employed during synthesis might cause deviations from expected stoichiometry. So, in present context where substitution dependent structural change is evident, it is essential to quantify the elemental composition of the system. Energy dispersive x-ray spectroscopy and x-ray photoelectron spectroscopy are used to determine the elemental composition, chemical state, and electronic state of the elements present in material.

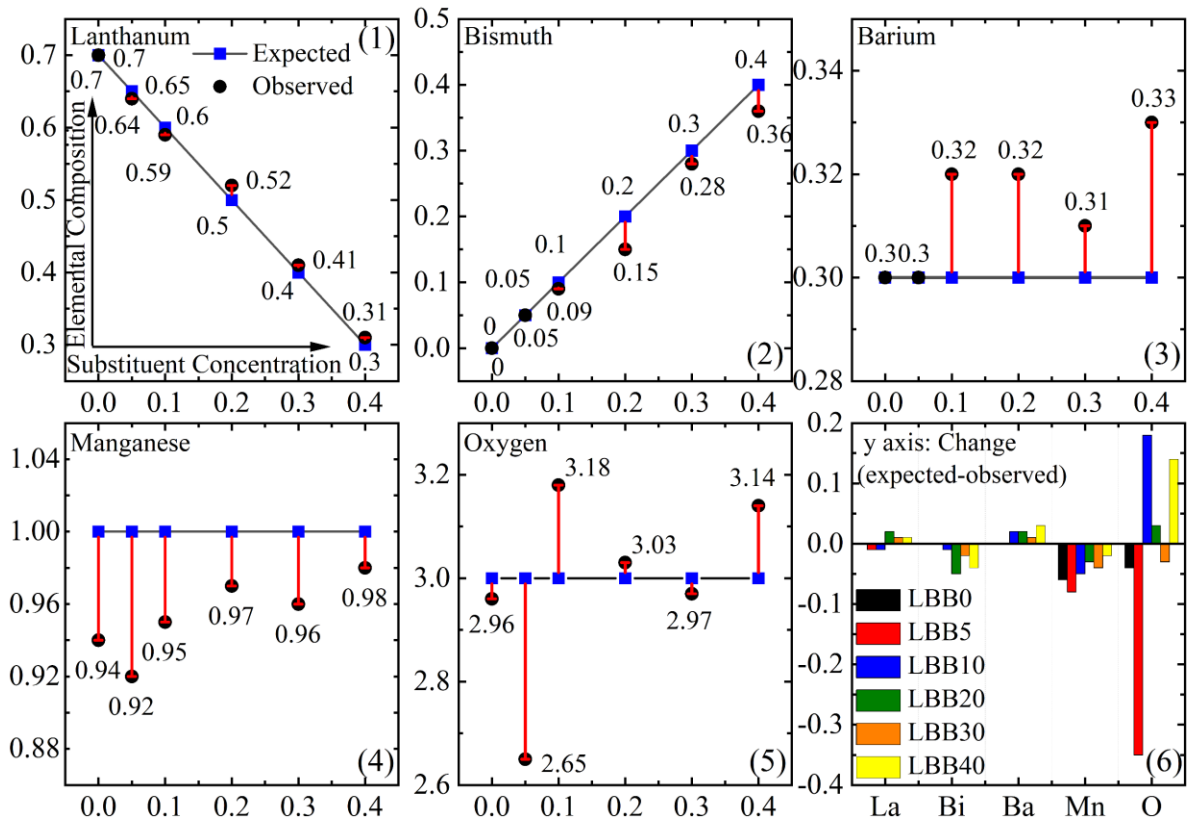


**Figure s7. The variation between the expected elemental composition and observed composition through EDS measurement.**

The spectra of each specimen taken over large area scan show desired elements along with the carbon. The atomic percentage of carbon found in measurement is nearly 25% indicating the surface purity is compromised. Upon interaction with high energy electron, the carbon emits characteristic x-rays which are similar in energy compared to the x-rays emitted by lighter elements such as oxygen. The overlap between the signals of carbon and oxygen may lead to inaccuracy in quantifying the atomic percentage of oxygen. The expected atomic percentage of oxygen in  $ABO_3$  perovskite is 60. But the atomic percentage received from EDS spans over 40-45% in all the sample. This leads to a speculation of some portion of the x-ray intensity of oxygen is shared with other element essentially carbon which is present at the surface of the specimen. Also, the presence of carbon can contribute to the high background

signal, which would obscure the signal coming from heavy elements leading into poor signal to noise ratio. Nevertheless, intense signals are seen from elements such as La, Mn, Ba, and Bi indicating the presence of the desired elements. Figure s7 depicts the estimated elemental composition against the expected composition. The panel 6 is self-explanatory on validity of elemental composition. The small height of the bar column in case of La, Bi, and Ba indicate the good agreement between the expected and observed elemental composition of A -site. In such situation, the composition of Mn (equal to 1) and O (equal to 3) should have been consistent with expected composition, but a large variation observed in atomic percentages is due to the ambiguity in signal detection and segregation due to their low atomic mass.

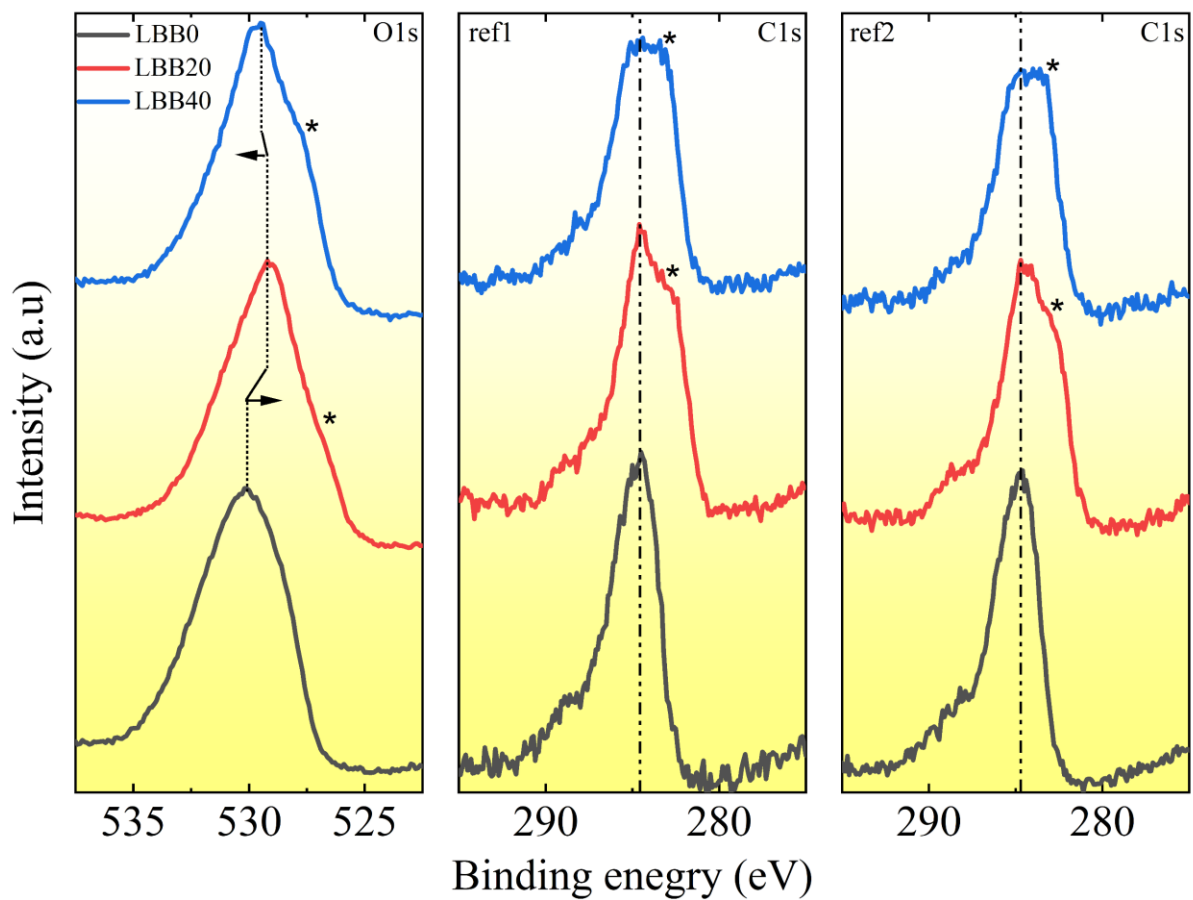


Figure s8. The XPS core level spectra of O 1s and C 1s for LBB0 to LBB40 laid bottom to top (ref 1 and ref 2 indicate the reference for charging correction taken before and after the scan)

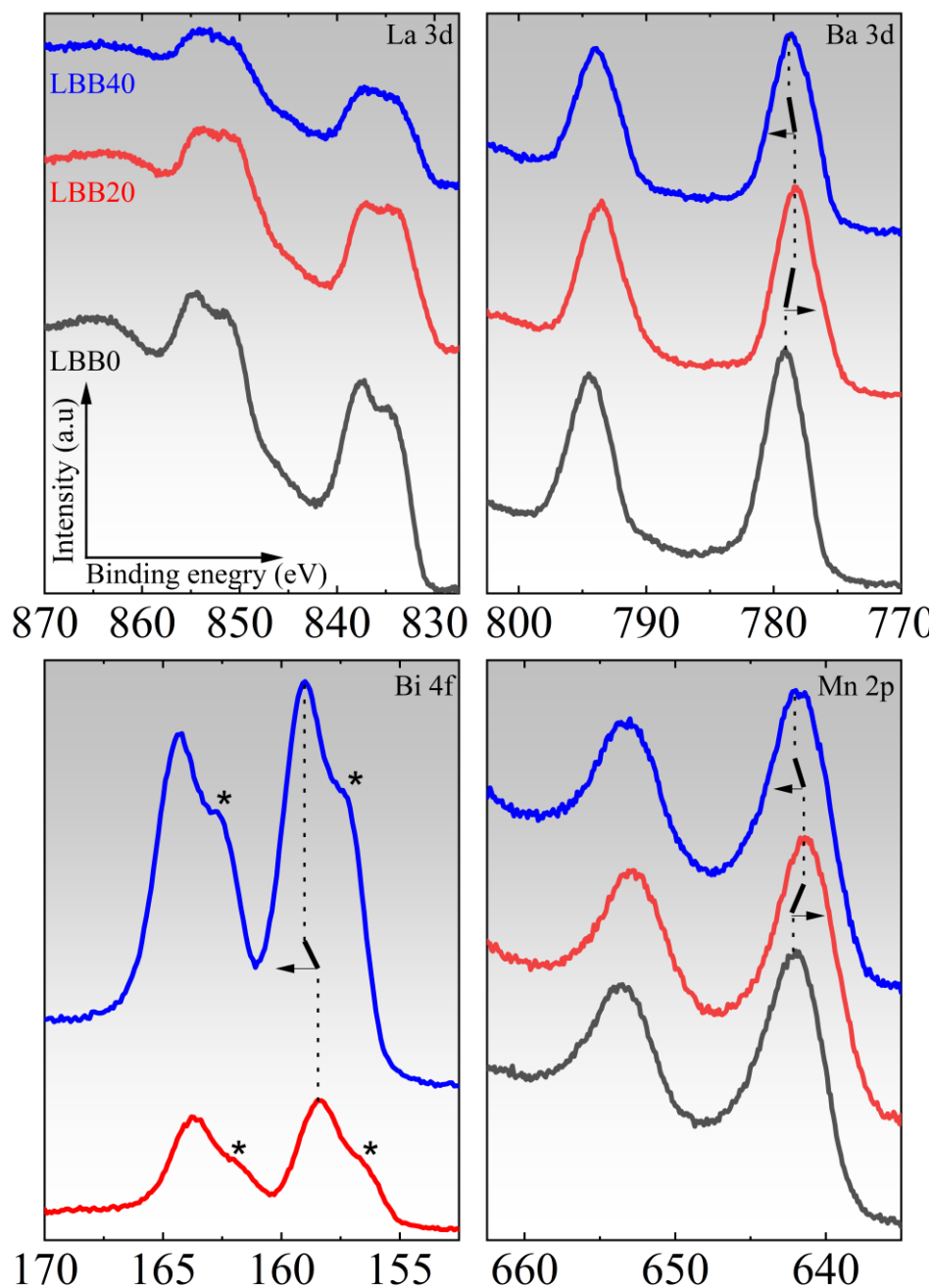
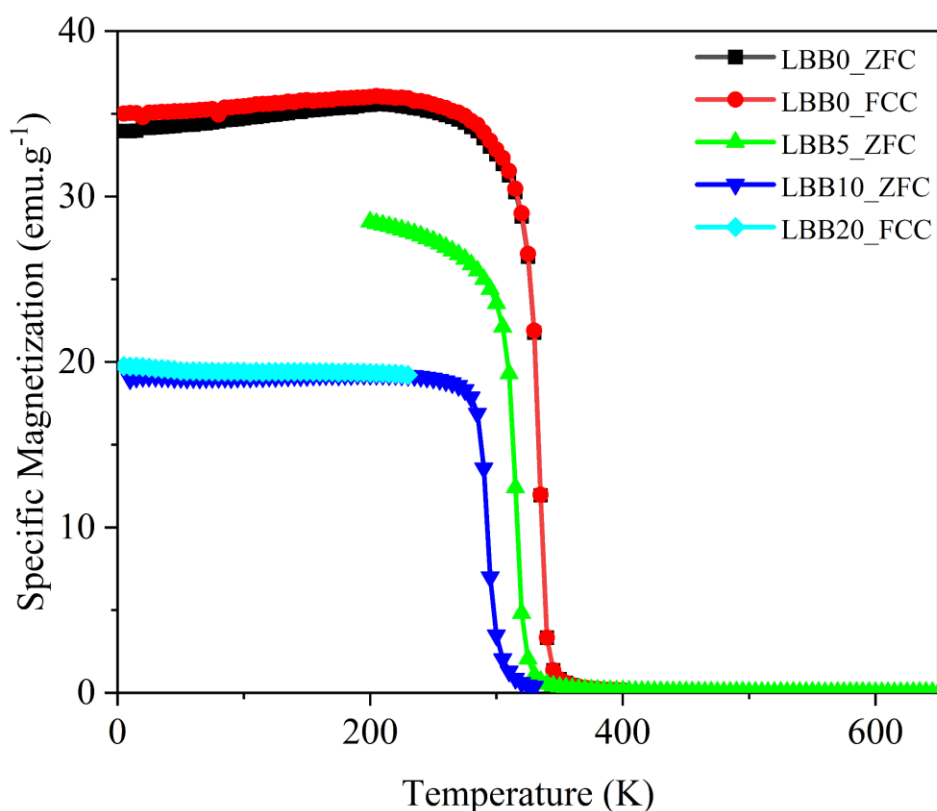


Figure s9. The XPS core level spectra of La 3d, Ba 3d, Bi 4f and Mn 2p for each specimen stacked for LBB0, LBB20 and LBB40 (bottom to top) respectively.

The survey spectra of XPS are merely employed for initial assessment and elemental identification. So being interim it cannot be used to comment on chemical state and chemical environment of the sample. Thus, a high-resolution spectrum or core spectrum is obtained for each element in the specimens and are displayed in figure s8 and s9. The second order derivative of each of these spectra can roughly estimate the peak positions and energy separation between SOS. In case of La 3d core spectra considering the lower energy component of SOS, main peaks are observed at 834.5eV, 833.5eV and 833.8eV and the satellites are observed at 837.6eV, 837.8eV and 837.7eV respectively for LBB0, LBB20, and LBB40. The B.E (B.E) separation for SOS are 16.6 eV for main peaks and 17.2 eV, 17 eV, and 17.4 eV for satellites. In case of Ba 3d the lower energy peaks of SOS are found at 778.9 eV, 778.0 eV, and 778.8 eV, the higher B.E peaks of SOS are found at 794.3 eV, 793.6 eV and 793.9 eV respectively (0 to 40%). The B.E separations are 15.4 eV, 15.6 eV, and 15.1 eV. In case of Bi 4f core level spectra the lower B.E SOS components are at 158.5eV, and 158.8eV whereas the higher B.E peaks are at 163.8eV and 164.4eV respectively for LBB20 and LBB40. The B.E separations are 5.3eV and 5.6eV respectively. The shoulder like features are seen at 156.4eV, 157.0eV (lower B.E) and 161.7eV, 162.4eV (higher B.E) respectively (20% to 40%). The separations are thus 5.3eV and 5.4eV. The manganese core SOS are seen at 641.9eV, 641.2eV, 641.6eV (major component of SOS) and 653.5eV, 652.7eV, 653.1eV (minor component of SOS) respectively for LBB0, LBB20 and LBB40. The BE separations are orderly 11.6eV, 11.5eV, and 1.5eV. The O 1s core level spectrum of LBB0 is asymmetric in nature and is found to develop a new feature at lower B.Es (marked by asterisk) upon Bi substitution. Similar is the case with C 1s core level spectra. The maximum of the O 1s core line is observed at 530.2eV, 529.1 eV and 529.8 eV respectively from LBB0 to LBB40. The shoulder in lower B.E are at 528.5eV, 526.7eV and 527.5eV respectively. Along with the said features, there are faint signals at approximately 531eV in all the spectra, the reliability of which is uncertain in

both LBB0 and LBB40. In case of C 1s, of course the main peaks are seen at 284.6eV due to carbon correction but a shoulder signal is seen at  $\approx 289.0\text{eV}$  in all the spectra. Interestingly the emergence of new feature at lower B.E upon Bi substitution is seen at 282.5eV and 283.0eV respectively for LB20 and LB40. Intriguingly the core lines of Ba-3d, Mn-2p, and O-1s shift towards the lower B.Es except for bismuth. Having known the B.E positions and separations, to assign each of these features, to understand precise variation in their B.Es upon Bi substitution, and to understand different type of chemical bonding involved in structure formation, a deconvolution is carried out using CasaXPS peak fitting software.



**Figure s10. The M versus T curves of LBB0, LBB5 and LBB10 in ZFC and FCC protocol.**

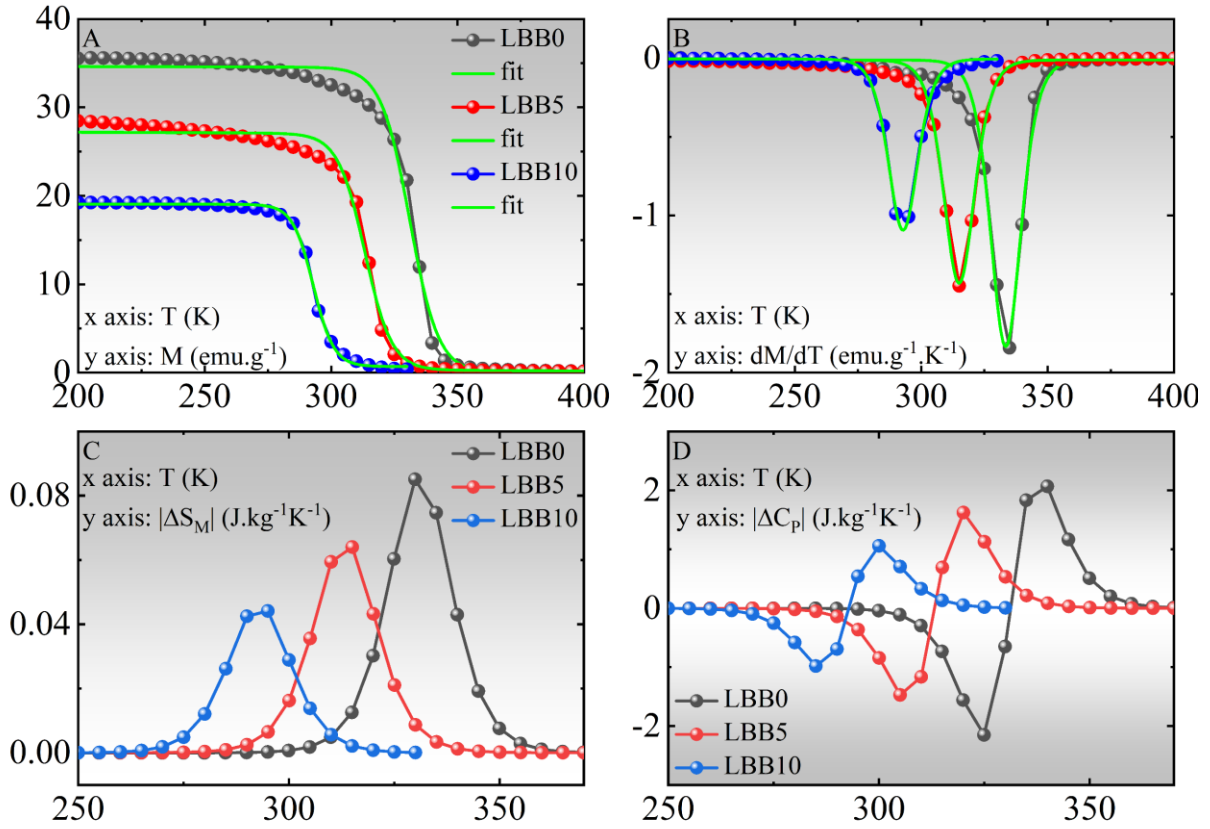


**Figure s11: The phenomenological fit given to temperature dependent magnetization (A) its first order derivative (B), the simulated entropy change (C) and simulated change in specific heat (D).**

The phenomenological model is one of the analysis routes for estimating the magnetic entropy change  $\Delta S_M$ . The shortcomings of the model have been brought out by R. Zouari *et al*<sup>22</sup>. where the authors conclude lack of rigorous estimate of MCE in ferromagnetic material by the model. However, many researchers have successfully exploited the model and validated the agreement between the experimental results and simulation performed under the governance of model particularly at low magnetizing intensities. The phenomenological model was proposed by M.A. Hamad<sup>23</sup> according to which magnetization of a ferromagnetic material varies with temperature as  $M(T) = \left\{ \left( \frac{M_i - M_f}{2} \right) \times \tanh (A \times (T_C - T)) \right\} + BT + C$ . Here,  $M_i$  is the value of magnetization in the FM state,  $M_f$  is the magnetization in PM state,  $T_C$  is the curie

temperature and  $A$ ,  $B$ ,  $C$  are constants for a given material,  $A = \frac{2 \times (B - S_C)}{(M_i - M_f)}$  and  $C = \frac{(M_i + M_f)}{2} - BT_C$ .  $B$  stands for magnetization sensitivity ( $\frac{dM}{dT}$ ) prior transition, and  $S_C$  is the magnetization sensitivity at  $T_C$ . The magnetic entropy change is given by  $\Delta S_M = \left[ \left\{ -A \times \left( \frac{M_i - M_f}{2} \right) \times \text{sech}^2(A \times (T_C - T)) \right\} + B \right] \times H_M$  and magnetic contribution to change in specific heat given by  $\Delta C_P = -2TA^2 \times \left( \frac{M_i - M_f}{2} \right) \times \text{sech}^2(A \times (T_C - T)) \times \tanh(A \times (T_C - T)) \times H_M$ . The detailed discussion on the model can be found in our earlier studies<sup>24</sup>. Figure s10 depicts the phenomenological fit given to the experimental data (figure s10 A, B) to extract the fit parameter  $M_i$ ,  $M_f$ ,  $T_C$ ,  $B$ , and  $S_C$ . These values are utilised to simulate  $\Delta S_M$  and  $\Delta C_P$ . The simulated curves are shown in fig s10 C and D. The estimated values of  $A$ , maximum of the entropy change ( $|\Delta S_M^{\max}|$ ), the full width at half maxima ( $\delta T_{\text{FWHM}}$ ), the relative cooling power (RCP) and minimum and maximum of the specific heat change  $\Delta C_P^{\min}$ ,  $\Delta C_P^{\max}$  are tabulated in table s6

**Table s6: fit parameters of phenomenological model and thermomagnetic physical quantises.**

<b>X</b>	$M_i$ ( <i>emu.g<sup>-1</sup></i> )	$M_f$ ( <i>emu.g<sup>-1</sup></i> )	$B \times 10^{-4}$ ( <i>emu.g<sup>-1</sup>K<sup>-1</sup></i> )	$S_C$ ( <i>emu.g<sup>-1</sup>K<sup>-1</sup></i> )	$T_C$ ( <b>K</b> )
<b>0</b>	34.5 <sup>a</sup>	0.0 <sup>a</sup>	-6 <sup>a</sup>	-1.5 <sup>a</sup>	331.1 <sup>a</sup>
	34.5 <sup>b</sup>	5.0 <sup>b</sup>	0 <sup>b</sup>	-1.8 <sup>b</sup>	333.4 <sup>b</sup>
<b>0.05</b>	27.1	0.3	-12	-1.3	313.3
	27.1	3.8	-110 <sup>b</sup>	-1.4	315.0
<b>0.1</b>	19.0	0.7	-3	-1.1	292.9
	17.8	0.7	-46.9	-1.1	292.9
<b>Thermomagnetic Parameters</b>					

<b>X</b>	<b>A</b> ( $K^{-1}$ )	$ \Delta S_M^{max} $ $\times 10^{-3}$ ( $J.kg^{-1}K^{-1}$ )	$\delta T_{FWHM}$ ( $K$ )	<b>RCP</b> ( $J.kg^{-1}$ )	$\Delta C_P^{min}$ ( $J.kg^{-1}K^{-1}$ )	$\Delta C_P^{max}$ ( $J.kg^{-1}K^{-1}$ )
<b>0</b>	0.1	75	20.3	1.5	-2.1	2.1
	0.1	75	17.5	1.3	-1.7	1.9
<b>0.05</b>	0.1	65	14.8	1.2	-1.5	1.6
	0.1	70	14.9	1.0	-1.3	1.3
<b>0.1</b>	0.1	55	14.8	0.8	-1.0	1.1
	0.1	55	13.8	0.8	-0.9	1

a: fit parameter and thermomagnetic parameters estimated from magnetization curve, b: fit parameter and thermomagnetic parameters estimated from dM/dT curve

The adhere of fit to the M(T) and dM/dT and good agreement of fitting parameters  $M_i$ ,  $M_f$ ,  $T_C$ , B, and  $S_c$  in both approaches and the closeness of  $T_C$  estimated from methods of double derivative, Curie-Weiss fit, and phenomenological fit validated the agreement between chosen models. Notably the entropy change is maximum at  $T_C$  and drops of on either side. The value of  $-\Delta S_M$  is found to be positive in the entire temperature region. This implies release of heat in the process of magnetization and confirms the ferromagnetic nature of the specimens. Further with Bi substitution the maximum of  $\Delta S_M$ ,  $\delta T_{FWHM}$ , RCP, maximum and minimum  $\Delta C_P$  all reduce almost linearly expect for  $\delta T_{FWHM}$ .

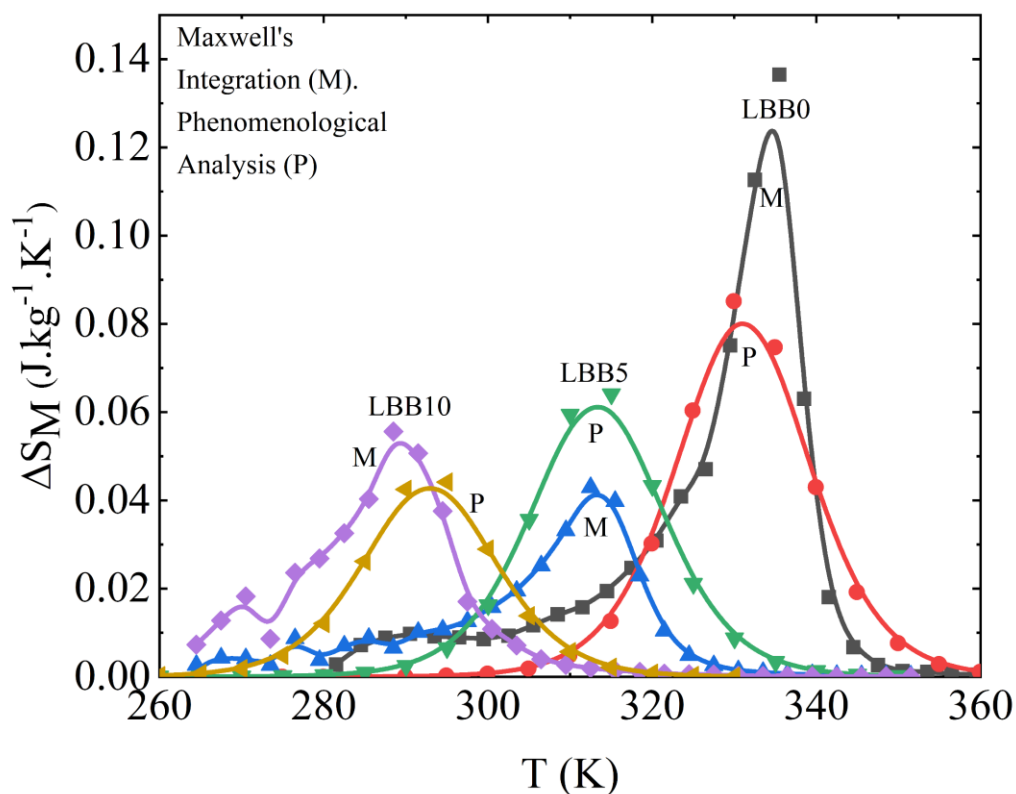


**Figure s12. The agreement between Maxwell's integration and phenomenological model.**

#### References

- 1 A. Le Bail, *Powder Diffraction*, 2005, **20**, 316–326.
- 2 A. M. Abdulwahab, *Int J Curr Res*, 2013, **5**, 2547–2553.
- 3 L. B. McCusker, R. B. Von Dreele, D. E. Cox, D. Louër and P. Scardi, *J Appl Crystallogr*, 1999, **32**, 36–50.
- 4 E. Y. Rha, J. M. Kim and G. Yoo, *Journal of Craniofacial Surgery*, 2015, **26**, e505–e506.
- 5 C. T. Rueden, J. Schindelin, M. C. Hiner, B. E. DeZonia, A. E. Walter, E. T. Arena and K. W. Eliceiri, *BMC Bioinformatics*, 2017, **18**, 1–26.
- 6 C. A. Schneider, W. S. Rasband and K. W. Eliceiri, *Nat Methods*, 2012, **9**, 671–675.
- 7 J. Schindelin, C. T. Rueden, M. C. Hiner and K. W. Eliceiri, *Mol Reprod Dev*, 2015, **82**, 518–529.

- 8 M. D. Abràmoff, P. J. Magalhães and S. J. Ram, *Biophotonics International*, 2004, **11**, 36–41.
- 9 T. J. Collins, *Biotechniques*, 2007, **43**, S25–S30.
- 10 Rishi Kumari and Narinder Rana, *International Journal of Engineering Research and*, 2015, **V4**, 247–250.
- 11 Northwestern University, 12.
- 12 M. Fátima Vaz and M. A. Fortes, *Scripta Metallurgica*, 1988, **22**, 35–40.
- 13 L. B. Kiss, J. Söderlund, G. A. Niklasson and C. G. Granqvist, *Nanotechnology*, 1999, **10**, 25–28.
- 14 J. Söderlund, L. B. Kiss, G. A. Niklasson and C. G. Granqvist, *Phys Rev Lett*, 1998, **80**, 2386–2388.
- 15 G. W. Petty and W. Huang, *J Atmos Sci*, 2011, **68**, 1460–1473.
- 16 M. F. Vaz and M. A. Fortes, *Scripta Metallurgica*, 1988, **22**, 35–40.
- 17 T. Ishihara, *Perovskite Oxide for Solid Oxide Fuel Cells*, Springer US, 2014.
- 18 G. George, S. R. Ede and Z. Luo, *Fundamentals of Perovskite Oxides*, CRC Press, 2020.
- 19 M. B. Salamon and M. Jaime, *Rev Mod Phys*, 2001, **73**, 583–628.
- 20 H. Gencer, S. Atalay, H. I. Adiguzel and V. S. Kolat, *Physica B Condens Matter*, 2005, **357**, 326–333.
- 21 K. Sun, Z. Lan, Z. Yu, L. Li, J. Huang and X. Zhao, *J Phys D Appl Phys*, DOI:10.1088/0022-3727/41/23/235002.
- 22 R. Zouari and A. Chehaidar, *Phase Transitions*, 2017, **90**, 167–174.
- 23 M. A. Hamad, *Phase Transitions*, 2012, **85**, 106–112.
- 24 L. D. Mendonca, M. S. Murari and M. D. Daivajna, *J Supercond Nov Magn*, 2021, **34**, 2067–2078.